PHYSICAL REVIEW B **76**, 035209 (2007)

# Composition-dependent electronic properties, optical transitions, and anionic relaxations of $Cd_{1-x}Zn_xTe$ alloys from first principles

He Duan, Xiaoshuang Chen,[*,†] Yan Huang, Xiaohao Zhou, Lizhong Sun, and Wei Lu[*,‡]
*National Laboratory for Infrared Physics, Shanghai Institute of Technical Physics, Chinese Academy of Sciences, 200083 Shanghai, People's Republic of China*

(Received 21 June 2006; revised manuscript received 3 February 2007; published 24 July 2007)

We have investigated the ionic relaxations, electronic structures, and optical properties for $Cd_{1-x}Zn_xTe$ alloys using density functional theory. The quasi-zinc-blende structure is used with special emphasis on the relaxation behaviors of $Te^{2-}$ around either $Cd^{2+}$ or $Zn^{2+}$. Our calculations confirm that the relaxations of the anion rather than the cation contribute primarily to the alloying process as predicated by the experiments. The differences in the ionicity of $Cd^{2+}$ and $Zn^{2+}$ and their configurations around $Te^{2-}$ are responsible for the different relaxation behaviors of $Te^{2-}$. A striking result is the relevance of the relaxation behaviors of $Te^{2-}$ with the alloying effect on the electronic states. This result supports the electronic features of $Cd_{0.5}Zn_{0.5}Te$ alloy reported by the systematic analyses with quasirandom structure. The band structures obtained here are used to determine the optical functions. The comparison with the available experimental and theoretical results suggests an overall topological resemblance in the present dielectric function spectra when the band-gap correction is included.

DOI: 10.1103/PhysRevB.76.035209 PACS number(s): 71.20.Nr, 71.23.An, 72.10.Bg

## I. INTRODUCTION

Among alloy semiconductors by large size-mismatched binaries, $Cd_{1-x}Zn_xTe$ has attracted particular interest in the fabrication of detectors[1–3] for x rays, beta rays, gamma rays, cosmic rays, high-energy radiation, and infrared electromagnetic radiation in medical imaging.[4] Excellent photosensitivity and high resistivity are its main features.[5,6] To upgrade the radiation detector performance, intrinsic material with high crystalline perfection and high resistivity is required. Although the intrinsic resistivity of $Cd_{1-x}Zn_xTe$ alloys increases monotonously with the increase of the zinc mole fraction $x$, the crystalline perfection shows degradation due to the incorporation of impurities and defects at increased melt temperature, which deteriorates the alloy's electronic and optical properties.[7] Hence, the reliable experimental information about $Cd_{1-x}Zn_xTe$ alloys $(x>0.2)$ with desired properties is scarce. In addition, $Cd_{1-x}Zn_xTe$ is also a leading material as substrates or passivation layers for the epitaxial growth of HgCdTe infrared detector material[8,9] because of the improved properties of the interface. Therefore, knowledge of the optical constants of CdZnTe alloys is of great interest in the design and analysis of passivating HgCdTe. These factors make theoretical studies a necessary addition to experimental investigations for the advancement of the detector technology.

Early studies[10–16] have suggested that lattice distortions may occur in semiconductor alloys composed of size-mismatched compounds. When considering $Cd_{1-x}Zn_xTe$ alloys, the ionic relaxations have been confirmed experimentally by extended x-ray-absorption fine-structure[17] and nuclear magnetic resonance measurements.[18] On the other hand, the geometrical deformation around the lattice sites of alloys correspondingly leads to the mixing or preservation of the characteristic features in the electronic states of the binary constituents. This has been understood for $Cd_{1-x}Zn_xTe$ alloys with $x=0.5$ by three major models, namely, the virtual crystal approximation,[19,20] the site-coherent potential approximation,[21,22] and the quasirandom structure (SQS) model.[23–25] In the SQS model, $Cd^{2+}$ and $Zn^{2+}$ are statistically distributed in short range. It was used by Wei and Zunger in their systematic studies of the cation disorder effects on the splitting and broadening of the electronic states. This model was examined by the angle-resolved valence-band photoemission spectrum.[26] In addition, experiments have also shown that the anion sublattice has a much stronger distortion than the cation sublattice in zinc-blende-type $A_{1-x}B_xC$ alloys.[27] Therefore, the structural and electronic properties of $Cd_{1-x}Zn_xTe$ alloys are expected to be relevant to the anionic relaxations. In order to understand this, the cation disorder effects are ignored here with special emphasis on the relaxation behaviors of $Te^{2-}$ around either $Cd^{2+}$ or $Zn^{2+}$ in periodical but nonstatistical distribution. Such consideration is justified in reasonably describing the relaxations of $Te^{2-}$ around $Cd^{2+}$ or $Zn^{2+}$, the electronic structures, and the trend in alloying properties with composition.

Meanwhile, knowledge of the optical properties of the technologically important material $Cd_{1-x}Zn_xTe$ is of great interest in effectively evaluating the quality of the given samples and in the design and processing of passivating HgCdTe focal plane arrays by means of accurately predicting optical response. Different experimental techniques have been employed to measure the optical properties in $Cd_{1-x}Zn_xTe$ material, such as spectroscopic ellipsometry,[28,29] photoluminescence spectra,[30] and Raman spectra.[31] The spectroscopic ellipsometry permits direct measurements of the real and imaginary parts of the pseudodielectric function $\varepsilon(\omega)$ and dielectric related optical constants.[32,33] The corresponding optical functions are modeled to facilitate the experimental analysis at the same time.[34–36] These numerical models reasonably described the given samples but depended heavily on the assumed fitting parameters. As a consequence, different models gave consistent critical peak positions on the premise of different sets of fitting parameters. Although the optical properties of CdTe and ZnTe binaries have been characterized,[37] information about the related ternaries is very limited.[38,39] Besides, the first-principles optical calculations for $Cd_{1-x}Zn_xTe$ ternaries are still lacking, to our knowledge, except for detailed theoretical works on binaries[40–43] as well as recent experimental investigations.[44,45]

In this work, we initially study the dominant role of $Te^{2-}$ relaxations in the alloying process for $Cd_{1-x}Zn_xTe$ ternaries from the first-principles calculations. Then, we demonstrate that the alloying effect on the electronic states is relevant to the relaxation behaviors of $Te^{2-}$. Finally, we use the band calculations to explain the main features in optical-related functions. The purpose of this work is to account for the following: (1) the relaxation behaviors for $Cd_{1-x}Zn_xTe$ ternaries with different compositions, (2) the alloying effect on the electronic states from the viewpoint of the relaxations of $Te^{2-}$ instead of the cation disorder as emphasized in previous studies, and (3) the optical transition mechanisms and the variations of optical response in terms of alloy composition, especially for ternaries.

## II. DETAILS OF THE CALCULATIONS

The present calculations were carried out using fully relativistic (i.e., including spin-orbital coupling through a second variational procedure[46]) full-potential augmented plane wave plus local orbital[47] method in generalized gradient approximation[48] incorporated in the WIEN2K code. We constructed $2\times1\times1$ supercells of 16 atoms, twice the size of the quasi-zinc-blende unit cell. We determined the equilibrium lattice constants based on the principle of total energy minimum. Firstly, an isotropic compression and expansion of the unit cell was made to create uniform variation in terms of the initial volumes $V_0$. The initial lattice constants were taken as the experimental values for binary compounds [e.g., 6.480 and 6.089 Å for CdTe and ZnTe (Ref. 49)], and for ternary compounds they were taken as an analytical interpolation between the experimental values of the constituents by Vegard's rule. Then, the total energy ($E$) for a set of unit cell volume ($V$) was calculated, and the obtained $E$ versus $V$ data were fitted to Murnaghan's equation of state,[50] meaningful in a physical sense as an effective tool to describe the dependence of the total energies on the lattice volume. Finally, we interpolated the value of the minimum $E_{min}(V_{eq})$ from the fitted $E$ versus $V$ curves. When the step size was reduced to ±0.5% around $V_0$, Murnaghan's equation of state (EOS) fitting results were in good agreement with that of the total energy minimum (which requires considerably fine $E$ versus $V$ data with the step size being ±0.1%) and ensured an accuracy of 0.01 Å in equilibrium lattice constant. Thus, the fitting results were 6.483 and 6.101 Å for CdTe and ZnTe, and 6.388, 6.293, and 6.218 Å for ternaries with $x=0.25$, 0.5, and 0.75, respectively. Then, the fitting results for ternaries were subjected to the geometry optimization to obtain the equilibrium atomic positions with respect to the cell internal coordinates. The atomic positions in ternary supercells were fully relaxed using the reverse-communication trust-region quasi-Newton method from the PORT library[51,52] until the force on the atoms was below 0.05 eV/Å.

The parameters tested for self-consistency were the following: The inner-shell electrons were distinguished from the valence electrons of Cd $(4d^{10},5s^2)$, Zn $(3d^{10},4s^2)$, and Te $(5s^2,5p^4)$ by proper separation energy. The local orbitals were introduced as semicore states for Cd $4p$, Zn $3p$, and Te $4d$. No shape approximations were made on the crystal potential and charge density. The same values of the muffin-tin radii were used for anion and cation atoms for a given structure. In order to ensure a least charge leakage out of the muffin-tin spheres, we chose the sphere radii being slightly less than the nearest-neighbor distances (which were derived from volume optimizations) for binaries, 2.65 a.u. for CdTe and 2.45 a.u. for ZnTe. When the above considerations were applied to the ternary alloys, the large lattice mismatch between ZnTe and CdTe further prevented the use of larger muffin-tin spheres. We further reduced the sphere radii by about 6%–8% from the nearest-neighbor distances of the prerelaxed structures in order to avoid the occurrence of an overlapping or a collision of the muffin-tin spheres during the lattice relaxations; thus, they were fixed at 2.45 a.u. for $Cd_{0.75}Zn_{0.25}Te$, 2.35 a.u. for $Cd_{0.5}Zn_{0.5}Te$, and 2.35 a.u. for $Cd_{0.25}Zn_{0.75}Te$, respectively, during this procedure. All the sphere radii were also kept the same in the self-consistent calculations for both prerelaxed and relaxed ternaries in order to reduce random errors (which would otherwise produce slightly different total energies per atom of the same alloys). The value of $R_{MT}K_{max}$, controlling the size of the basis set, was kept at 8.0 (equivalent to about 11 Ry). Such a large cutoff energy is required because of the localized $d$ orbitals and the requirement of nonoverlapping muffin-tin spheres for the linearized augmented plane wave method. The nonspherical potential and charge density are expanded inside the muffin-tin spheres in terms of lattice harmonics up to $l=6$. The **k** point used for integrations was a $6\times12\times12$ Monkhorst-Pack mesh (436 points with no inversion in the irreducible wedge). All of the above parameters ensured an accuracy of 0.01 mRy in total energy. After the self-consistency is reached, the energy eigenvalues and vectors were recalculated at a dense mesh of uniformly distributed **k** points (1000 points), to be used for the calculations of the optical transition functions.

In order to verify the results of the 16-atom supercells, larger supercells with 64-atoms were adopted in the calculations of the ionic relaxations. In the case of 64-atom supercells, all the sphere radii were kept the same as that for 16-atom supercells. $R_{MT}K_{max}=6.0$ (equivalent to about 6.5 Ry) and $3\times3\times3$ Monkhorst-Pack mesh were used, and other parameters were kept same as that in the case of 16-atom supercells.

## III. RESULTS AND DISCUSSION

### A. Ionic relaxations in $Cd_{1-x}Zn_xTe$ alloys

The local geometry of the relaxed and prerelaxed ternaries is listed in Table I, together with that of bulk binaries for comparison. Note that the bond lengths obtained from the 16-atom supercell for $Cd_{0.5}Zn_{0.5}Te$ alloy (i.e., $d_{\text{Cd-Te}}=2.797$ Å and $d_{\text{Zn-Te}}=2.656$ Å for the 16-atom supercell) compare well with the values of the SQS-4 model[24,25] (i.e.,

TABLE I. Local geometry around $Cd^{2+}$ and $Zn^{2+}$ in $Cd_{1-x}Zn_xTe$ alloys in terms of the relaxed as well as the prerelaxed systems, compared with the same parameters of binary constituents. For each geometry parameter, the first line is for the 16-atom supercells, and the second line for the 64-atom supercells.

| | $x=0.25$ | | $x=0.5$ | | $x=0.75$ | | Binary | |
|---|---|---|---|---|---|---|---|---|
| | Prerelaxed | Relaxed | Prerelaxed | Relaxed | Prerelaxed | Relaxed | CdTe | ZnTe |
| $d_{\text{Cd-Te}}$ (Å) | 2.766 | 2.803 | 2.725 | 2.797 | 2.692 | 2.782 | 2.807 | |
| | | 2.799 | | 2.789 | | 2.772 | | |
| $d_{\text{Zn-Te}}$ (Å) | 2.766 | 2.659 | 2.725 | 2.656 | 2.692 | 2.652 | | 2.642 |
| | | 2.671 | | 2.663 | | 2.655 | | |
| $\alpha_{1(\text{Te-Cd-Te})}$ (deg) | 109.47 | 113.59 | 109.47 | 111.55 | 109.47 | 109.47 | 109.47 | |
| | | 113.13 | | 111.34 | | 109.47 | | |
| $\beta_{1(\text{Te-Cd-Te})}$ (deg) | 109.47 | 107.45 | 109.47 | 105.39 | 109.47 | 109.47 | 109.47 | |
| | | 107.67 | | 105.79 | | 109.47 | | |
| $\alpha_{2(\text{Te-Zn-Te})}$ (deg) | 109.47 | 109.47 | 109.47 | 113.77 | 109.47 | 111.52 | | 109.47 |
| | | 109.47 | | 113.33 | | 111.30 | | |
| $\beta_{2(\text{Te-Zn-Te})}$ (deg) | 109.47 | 109.47 | 109.47 | 107.36 | 109.47 | 105.44 | | 109.47 |
| | | 109.47 | | 107.58 | | 105.87 | | |

$d_{\text{Cd-Te}}=2.795$ Å and $d_{\text{Zn-Te}}=2.655$ Å) and the ZnTe/CdTe superlattices,[53] indicating good convergence of the 16-atom supercell for bond lengths. It can be seen that there is a little difference in the results of the 16-atom supercell and the 64-atom supercell, and that the relaxation magnitude is slightly smaller in the 64-atom structure than in the 16-atom one (i.e., within 0.02 Å and 0.5° for bond-length and bond-angle changes, respectively). The little difference is due to the reduced calculation accuracy used for the larger supercell (i.e., smaller $R_{\text{MT}}K_{\text{max}}$ and number of $\mathbf{k}$ points, and lower force convergence criteria). Since the two calculations show similar features in the structural relaxations, the 16-atom supercell will be used to describe the density of states and optical properties of $Cd_{1-x}Zn_xTe$ alloys in the following discussion.

It is shown that the bond lengths $d_{\text{Zn-Te}}$ and $d_{\text{Cd-Te}}$ are essentially conserved in $Cd_{1-x}Zn_xTe$ ternaries within 0.02 Å (or 1%) relative to bulk binaries despite the difference of 7.4% in the lattice constant between CdTe and ZnTe. It is therefore very interesting to investigate in detail how the cadmium ion ($Cd^{2+}$), the zinc ion ($Zn^{2+}$), and the telluride ion ($Te^{2-}$) in $Cd_{1-x}Zn_xTe$ alloys accommodate their positions in trying to conserve the binary bond lengths. During the alloying process of the $Cd_{1-x}Zn_xTe$ system, the higher fractional ionicity of $Cd^{2+}$ relative to $Zn^{2+}$ makes charges less bound with the former but more bound with the latter, which thus increases the radius of $Cd^{2+}$ while decreases that of $Zn^{2+}$. As a result, $Te^{2-}$ is left to adjust its position to accommodate the radius difference between $Cd^{2+}$ and $Zn^{2+}$ via relaxation. We find that there is a substantial outward expansion of the anion sublattice (about 12%), while the cation sublattices remain an overall undistorted fcc structure. Our results therefore support that it is the relaxations of $Te^{2-}$ rather than $Cd^{2+}$ and $Zn^{2+}$ that dominantly contribute to the alloying process as evidenced by the experiments.[27] We further investigate the relaxation behaviors as shown in Fig. 1. The inter-ionic stress stored in the prerelaxed structures pushes $Te^{2-}$ away from $Cd^{2+}$ to $Zn^{2+}$ as the result of the different cation radius during the relaxation process, which stretches the Cd-Te bond length and contracts the Zn-Te bond length at the same time, with the Cd-Te and Zn-Te bond lengths differing by about 0.14 Å.

There are two types of telluride ion in $Cd_{1-x}Zn_xTe$ alloys. One type ($Te_{(1)}$) is around $Cd^{2+}$ and the other type ($Te_{(2)}$) is around $Zn^{2+}$, leading to significant effects on the electronic structures (see later discussion). $Te^{2-}$ can be regarded as a combined effect of these two types of telluride ions. For $x=0.25$, each $Te_{(1)}$ is adjacent to an "isolated" $Zn^{2+}$ besides three $Cd^{2+}$ neighbors, whereas each $Te_{(2)}$ directly bonded to $Zn^{2+}$ is coordinated with three other $Cd^{2+}$. Both types of telluride ions are pushed toward $Zn^{2+}$ by total inter-ionic stress, but different local geometries around $Cd^{2+}$ and $Zn^{2+}$ are produced. The stress imposed on $Te_{(1)}$ leads to significant bond-angle distortion and Cd-Te bond stretching as a consequence of the deviation of the stress from the Cd-Te direction (denoted as arrows in Fig. 1). However, $Te_{(2)}$ undergoes such stress in the same direction as the Te-Zn bond, leading to an undistorted tetrahedron for $ZnTe_{(2)}$ with shorter bond lengths. The analogous behavior can be observed when $x=0.75$ except for the opposite stresses applied to $Te_{(1)}$ and $Te_{(2)}$. The distortion is significant in the $ZnTe_{(2)}$ tetrahedron but not in the $CdTe_{(1)}$ tetrahedron where only elongated Cd-Te bond lengths occur. Such behavior is relevant to the uneven cation distribution around telluride ions. Compared with these two cases, $Cd_{0.5}Zn_{0.5}Te$ alloy has a more even cation configuration. $Te_{(1)}$ and $Te_{(2)}$ are both subjected to stress along the angular bisector of two coplanar Te-Zn

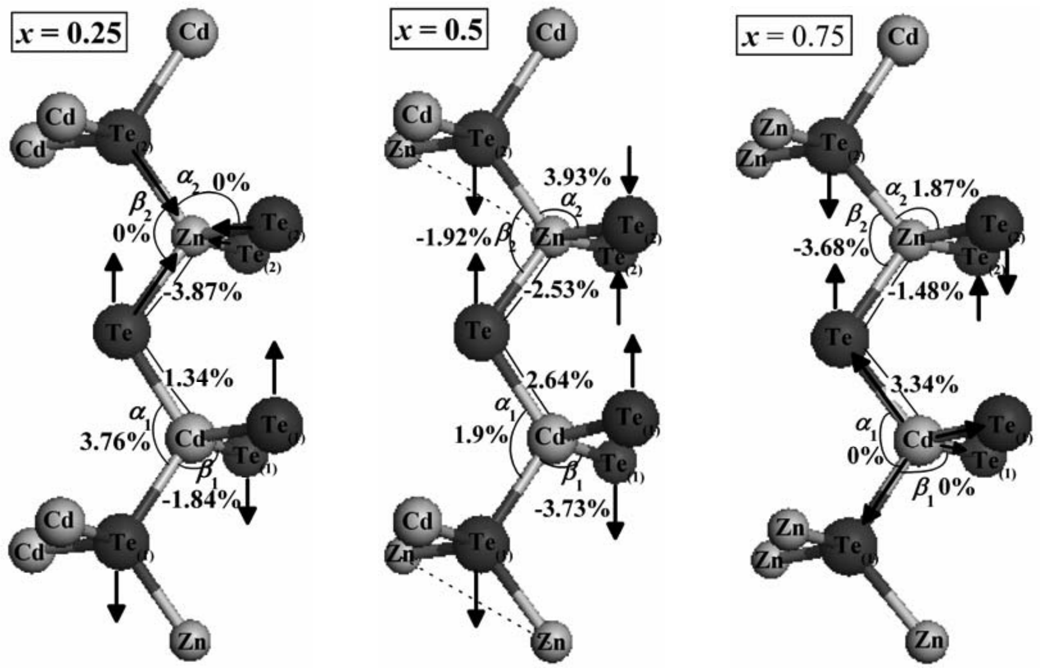

FIG. 1. The diagrammatic sketch of the relaxation behaviors of $Te_{(1)}$ and $Te_{(2)}$, coordinated around $Cd^{2+}$ and $Zn^{2+}$ in $Cd_{1-x}Zn_xTe$ alloys, respectively. The degree of distortion in the bond lengths and the bond angles is given in the percentage of the corresponding values in the prerelaxed structures. Arrows refer to the motion of telluride ions. Note that $Te^{2-}$ can be regarded as a combined effect of these two types of telluride ions.

bonds in order to adjust to the change of cation ionic radius. Thus, the isotropic distortion of the bond angles and bond lengths in $ZnTe_{(2)}$ and $CdTe_{(1)}$ tetrahedrons offsets the bond angle by ~2° for both α- and β-based bond angles. Furthermore, the $Te_{(1)}$ ion relaxes outward by 2.64% and the $Te_{(2)}$ ion inward by about the same extent (2.53% inward), respectively. However, the bond-length relaxations in both Cd-rich ($x=0.25$) and Zn-rich ($x=0.75$) cases exhibit considerable anisotropy. In the Cd-rich region, the dominant $Cd^{2+}$ pushes the telluride ions toward the $Zn^{2+}$, so that the contraction of Te-Zn bond is more significant (3.87% inward) than the stretching of the Te-Cd bond (1.34% outward). With an increase of the zinc mole fraction from 0.25 to 0.75, $Zn^{2+}$ dominates and pulls the telluride ions from $Cd^{2+}$ toward itself, so that the outward alternation of the Te-Cd bond lengths strikingly increases to 3.34% together with the dramatic decrease of Te-Zn bond-length alternation (1.48% inward). Interestingly, the bond-length relaxations in these two cases are complementary. It is also true for the bond-angle deformations: The $CdTe_{(1)}$ tetrahedrons in the $x=0.25$ alloy and $ZnTe_{(2)}$ in the $x=0.75$ alloy almost have equal bond angles on an average, i.e., 112° for the α-based bond angle and 106° for the β-based bond angle, respectively. Our calculated bond lengths in Table I agree with the theoretic prediction on the Cd-rich and Zn-rich cases.[54]

### B. Alloying effect on the electronic states of $Cd_{1-x}Zn_xTe$ ternaries

An important question is whether we can properly explain the alloying effect on the electronic states for $Cd_{1-x}Zn_xTe$ systems based on the above microscopic relaxation behavior. We therefore compare the total density of states (DOS) of the relaxed and prerelaxed structures in order to analyze the splitting and narrowing of electronic states induced by the ionic relaxations. Figure 2 depicts our results for the total DOS of the prerelaxed and relaxed structures for $x=0.25$, 0.5, and 0.75 $Cd_{1-x}Zn_xTe$ alloys, respectively. The overall total atomic DOSs of the relaxed structures are also given for identifying the orbital character enclosed within each DOS peak. Zero of energy is at the top of the valence band. Table II quantitatively gives the percentage of *s*, *p*, and *d* characters inside the muffin-tin sphere for each atom at Γ points. Figure 3 illustrates the charge densities associated with the characteristic peaks. Four regions labeled $P_1-P_4$ and two regions labeled $P_5$ and $P_6$ exist in the valence and in the lowest conduction band, respectively.

The deepest valence band denoted the $P_1$ region almost originates from Te 5*s* states with exceeding 70% percentage at the bottom of this region ($\Gamma_{1v}$). Since the wave functions of Te *s* states are atom centered, different configurations of $Te_{(1)}$- and $Te_{(2)}$-based tetrahedrons produce a splitting through Te-based sublattice deformation. In the prerelaxed structures, $Te_{(1)}$ and $Te_{(2)}$ *s* states are degenerate due to the absence of the Te-based sublattice deformation, and thereby, a single $P_1$ peak exists in this region. However, in the postrelaxed structures, a distinct splitting of the $P_1$ states into a high binding energy $P_{1(1)}$ and a low binding energy $P_{1(2)}$ is observed for Cd-rich ($x=0.25$) and Zn-rich ($x=0.75$) alloys. Inspection of the electronic charge densities in the $P_1$ region (e.g., $P_{1(1)}$ and $P_{1(2)}$ in Fig. 3 for $Cd_{0.25}Zn_{0.75}Te$ and $Cd_{0.75}Zn_{0.25}Te$) shows that the $P_{1(1)}$ peak is due to the tellu-

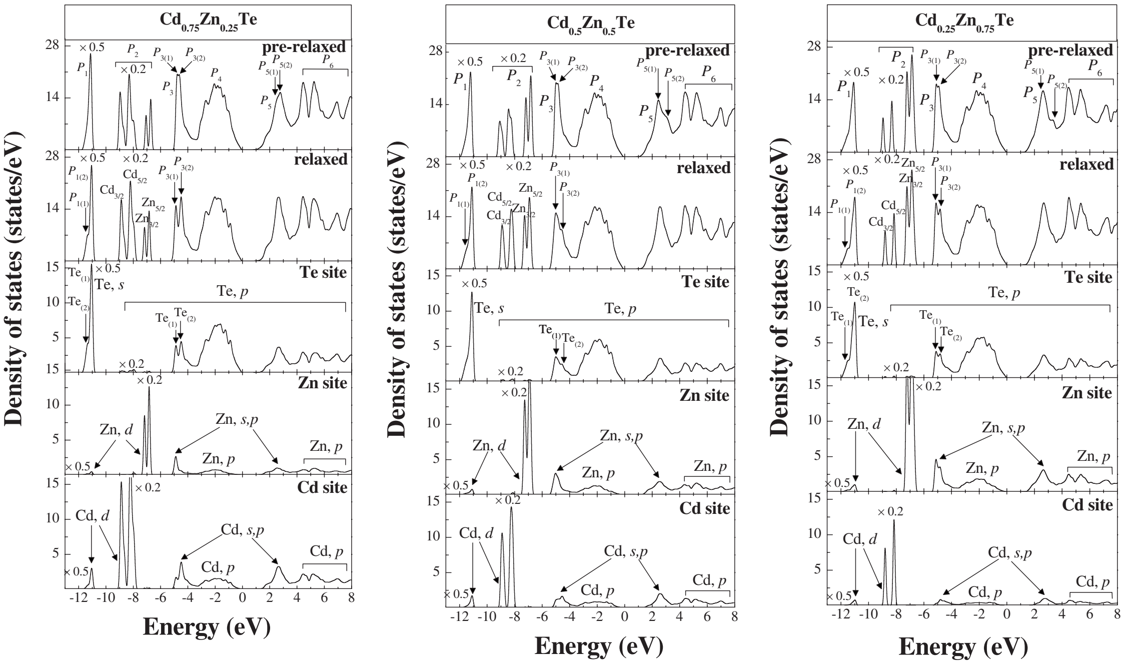

FIG. 2. Total and overall total atomic DOSs of the relaxed $Cd_{1-x}Zn_xTe$ alloys. Total DOS for the prerelaxed structures is plotted together to analyze the narrowing and splitting in electronic states induced by the ionic relaxations. Overall total atomic DOSs for Te, Zn, and Cd atom are given, respectively, for identifying the orbital character enclosed within each DOS peak. Zero of energy is at the top of the valence band.

ride ions around the minority cation ($Te_{(2)}$ for the Cd-rich case and $Te_{(1)}$ for the Zn-rich case), whereas the $P_{1(2)}$ peak is due to the telluride ions around the majority cation ($Te_{(1)}$ for the Cd-rich case and $Te_{(2)}$ for the Zn-rich case). The reason for this sequence of states can be appreciated as follows. Note from Fig. 1 that the telluride ions around the minority (majority) cation exhibit the tetrahedral deformation upon relaxation, associated with inter-ionic distance changes (angle deformation besides inter-ionic distance changes). This indicates that during the structural relaxation, the telluride ions around the majority cation have more freedom to adjust, and thereby, release larger part of the strain energy relative to the telluride ions around the minority cation. Consequently, the former-related *s* states move to shallower binding energies relative to the latter-related *s* states. The splitting observed in the $P_1$ region of $Cd_{0.25}Zn_{0.75}Te$ and $Cd_{0.75}Zn_{0.25}Te$ alloys corresponds to an evolution of these tetrahedron-deformation-shifted states. A relatively small $P_1$ splitting is found for $Cd_{0.5}Zn_{0.5}Te$ alloy, since in this case, the structural relaxation produces inter-ionic distance and angle deformation both in $Te_{(1)}$- and in $Te_{(2)}$-based tetrahedrons; hence, $Te_{(1)}$ and $Te_{(2)}$ *s* states are shifted to lower binding energies at the same time, modified slightly by their respective deformation potential. As indicated in Fig. 3 for $Cd_{0.5}Zn_{0.5}Te$, the wave-function amplitudes of the $P_{1(1)}$ states are qualitatively similar to those of the $P_{1(2)}$ states: the electronic charge densities are localized both on the $Te_{(1)}$ site and on the $Te_{(2)}$ site. This is consistent with the manifestation of SQS model[25] that the structural relaxation effects are small in the $P_1$ region for $Cd_{0.5}Zn_{0.5}Te$ alloy.

The metal *d* orbitals strongly contribute to the $P_2$ region. The dominant *d* character alternates between Cd 4*d* at the bottom side ($\Gamma_{8d},\Gamma_{7d}$) and Zn 3*d* at the top ($\Gamma_{8d}$) of this region in Table II, and the spin-orbit doublets ($j=3/2$ and $5/2$) of the metal *d* state are in the sequence $Cd_{3/2} < Cd_{5/2} < Zn_{3/2} < Zn_{5/2}$, determined from contrasting the total DOS and the overall total atomic DOS for Te, Zn, and Cd atoms. Our results are consistent with the theoretical studies by Wei and Zunger[25] and the *d*-state emission spectra[26] for $Cd_{0.5}Zn_{0.5}Te$ alloy.

From our calculations, the orbital energy of Zn 3*d* is 1.8 eV higher than Cd 4*d*, and the center of *d*-band energies is −7.10 and −8.31 eV for ZnTe and CdTe, which are in agreement with the values of 1.5, −7.18, and −8.31 eV given by Zunger and co-workers.[55,56] In their work, the chemical nature of the metal *d* states in $II^B$-VI semiconductors and the effect of the *d* states on the valence properties were systematically investigated. According to their well-established arguments, the *d* state binding energy ordering was reasonably attributed to the screening shift in the atomic-*d*-orbital energies. The screening contributions from the inner shells are equal because the added core shells from $^{30}Zn$ to $^{48}Cd$ completely screen the added 18 protons. Hence, one would expect the normal trend that the 3*d* states of the Zn atom should be lower in energy than the 4*d* states of the Cd atom. However, the screening contribution from the outmost *s* electrons is different because of the different penetrability. Compared with the Zn 4*s* wave functions, the added electron shells from Zn to Cd make the Cd 5*s* wave functions penetrate not as deep as the Zn 4*s* wave functions. Hence, the penetration of Cd 5*s* electrons worse shields the nucleus (thus more delocalized) compared with that of Zn 4*s* electrons, presenting Cd 4*d* electrons with a more attractive interaction with the atomic core (worse screened) relative to the Zn 3*d* electrons. Consequently, the increased binding of the outmost *s* orbitals

TABLE II. Percentage of $s$, $p$, and $d$ characters in the muffin-tin spheres. The first line is for Te atom, the second for Zn atom, and the third for Cd atom. The total charge of a state enclosed in the atomic spheres ("total charge") is given too.

| | $x=0.25$ | | | | $x=0.5$ | | | | $x=0.75$ | | | |
|---|---|---|---|---|---|---|---|---|---|---|---|---|
| State | $s$ (%) | $p$ (%) | $d$ (%) | Total charge | $s$ (%) | $p$ (%) | $d$ (%) | Total charge | $s$ (%) | $p$ (%) | $d$ (%) | Total charge |
| $\Gamma_{6v}$ | 51.3 | 0 | 0 | 2.3 | 77.0 | 0 | 0 | 6.3 | 77.2 | 0 | 0 | 6.2 |
| | 30.3 | 0 | 0 | 1.4 | 14.4 | 0 | 0 | 1.2 | 14.1 | 0 | 0 | 1.2 |
| | 16.6 | 0 | 0.2 | 0.8 | 7.8 | 0 | 0.1 | 0.7 | 8.0 | 0 | 0 | 0.7 |
| $\Gamma_{8d}$, | 0 | 0.9 | 0 | 0.3 | 0 | 0.5 | 0 | 0.2 | 0.3 | 0.2 | 0 | 0.2 |
| $\Gamma_{7d}$ | 0 | 0 | 0.2 | 0.1 | 0 | 0 | 0 | 0 | 0.2 | 0 | 0.1 | 0.2 |
| | 0 | 0 | 98.8 | 30.9 | 0 | 0 | 99.4 | 45.9 | 0 | 0 | 99.2 | 11.6 |
| $\Gamma_{8d}$ | 0.6 | 0.2 | 0 | 0.4 | 0.7 | 0.1 | 0 | 0.2 | 1.3 | 0.2 | 0 | 0.3 |
| | 0 | 0 | 98.0 | 45.2 | 0 | 0.1 | 99.2 | 22.7 | 0 | 0.2 | 93.1 | 14.8 |
| | 0 | 0 | 1.1 | 0.5 | 0 | 0.1 | 2.7 | 0.7 | 0 | 0.2 | 5.0 | 0.9 |
| $\Gamma_{7v}$, | 0 | 76.1 | 0 | 11.9 | 0 | 73.3 | 0 | 2.9 | 0 | 71.8 | 0 | 11.8 |
| $\Gamma_{8v}$ | 0 | 4.2 | 7.5 | 1.9 | 0 | 5.3 | 6.8 | 1.0 | 0 | 5.1 | 7.3 | 2.1 |
| | 0 | 5.3 | 6.0 | 1.8 | 0 | 4.4 | 9.5 | 1.2 | 0 | 6.6 | 8.6 | 2.6 |
| $\Gamma_{6c}$ | 0 | 0 | 0 | 0 | 0.1 | 0 | 0 | 0 | 0.3 | 0.1 | 0 | 0.1 |
| | 57.3 | 0 | 0 | 5.4 | 61.5 | 0 | 0.1 | 5.2 | 68.4 | 0 | 0.2 | 5.2 |
| | 41.2 | 0 | 0.1 | 3.9 | 36.8 | 0 | 0.2 | 3.2 | 29.3 | 0 | 0 | 2.3 |
| $L_{6v}$ | 0.1 | 51.4 | 13.6 | 5.7 | 0 | 65.3 | 0 | 5.2 | 0 | 67.9 | 0 | 5.9 |
| | 7.7 | 3.3 | 6.0 | 1.5 | 6.1 | 3.2 | 7.4 | 1.4 | 0.9 | 3.7 | 8.9 | 1.2 |
| | 6.0 | 4.5 | 6.6 | 1.5 | 4.3 | 5.4 | 7.6 | 1.4 | 0.7 | 6.1 | 11.1 | 1.6 |
| $L_{6v}$, | 0 | 72.9 | 0 | 6.4 | 0 | 73.0 | 0 | 5.9 | 0 | 68.0 | 0 | 11.3 |
| $L_{4,5v}$ | 0 | 4.1 | 6.9 | 1.0 | 0 | 5.5 | 6.7 | 1.0 | 2.8 | 5.0 | 6.9 | 2.5 |
| | 0 | 4.6 | 8.1 | 1.1 | 0 | 4.6 | 9.4 | 1.2 | 1.9 | 6.4 | 8.3 | 2.8 |
| $L_{6c}$ | 0 | 11.0 | 0 | 1.1 | 0.1 | 8.6 | 0 | 0.8 | 0.4 | 9.6 | 0 | 0.8 |
| | 49.5 | 0.6 | 0.8 | 4.8 | 55.5 | 0.2 | 0.9 | 4.8 | 61.8 | 0.4 | 1.0 | 4.8 |
| | 34.9 | 0.8 | 0.8 | 3.4 | 31.9 | 0.8 | 0.6 | 2.8 | 24.0 | 0.6 | 0.6 | 2.0 |
| $X_{7v}$ | 0.3 | 64.7 | 0 | 11.2 | 0.1 | 63.7 | 0 | 10.2 | 0.1 | 61.4 | 0 | 10.2 |
| | 4.8 | 5.0 | 6.0 | 2.8 | 4.3 | 5.0 | 6.5 | 2.6 | 4.5 | 6.4 | 6.6 | 3.0 |
| | 4.1 | 6.7 | 7.5 | 3.2 | 3.7 | 7.3 | 8.7 | 3.2 | 3.8 | 8.5 | 8.1 | 3.4 |
| $X_{6v}$, | 0 | 70.3 | 0 | 11.7 | 0 | 68.2 | 0 | 10.7 | 0 | 65.7 | 0 | 10.6 |
| $X_{7v}$ | 0 | 7.5 | 5.9 | 2.3 | 0 | 7.8 | 6.3 | 2.3 | 0 | 9.0 | 6.2 | 2.5 |
| | 0 | 8.4 | 7.1 | 2.6 | 0 | 8.9 | 8.0 | 2.7 | 0 | 10.5 | 7.9 | 3.0 |
| $X_{6c}$ | 3.0 | 29.3 | 0 | 6.4 | 0.8 | 25.3 | 0 | 4.8 | 0.8 | 23.8 | 0 | 4.3 |
| | 41.2 | 1.5 | 1.3 | 8.7 | 60.7 | 0.4 | 2.2 | 11.4 | 68.3 | 2.3 | 1.9 | 12.6 |
| | 19.5 | 1.6 | 0.9 | 4.4 | 7.7 | 0.8 | 1.0 | 1.8 | 0 | 0.5 | 1.3 | 0.4 |

(e.g., by 0.32 eV from Cd 5$s$ to Zn 4$s$ in our calculations, comparable with the value of 0.27 eV given in Ref. 54) is associated with a decrease in the binding of outer $d$ electrons from Cd to Zn. As the outer $d$ electrons become shallower from Cd to Zn, they approach more closely the energies of the Te $p$ states, causing a stronger $p$-$d$ overlap interaction in ZnTe relative to CdTe. This effectively increases the contribution of the $d$ states to the cohesive energy in ZnTe relative to CdTe. This is the main reason why ZnTe (which has more chemically active, open-shell 3$d$ orbitals) has a larger cohesive energy than CdTe (e.g., by 0.26 eV in our calculations, in agreement with the value of 0.29 eV given in Ref. 55). On the other hand, since Zn and Cd have delocalized $d$ orbitals, the $d$-state binding energy ordering for Zn and Cd depends on the calculation methods. Comparing our results with that of Wei and Zunger,[55] good agreement is found by consider-

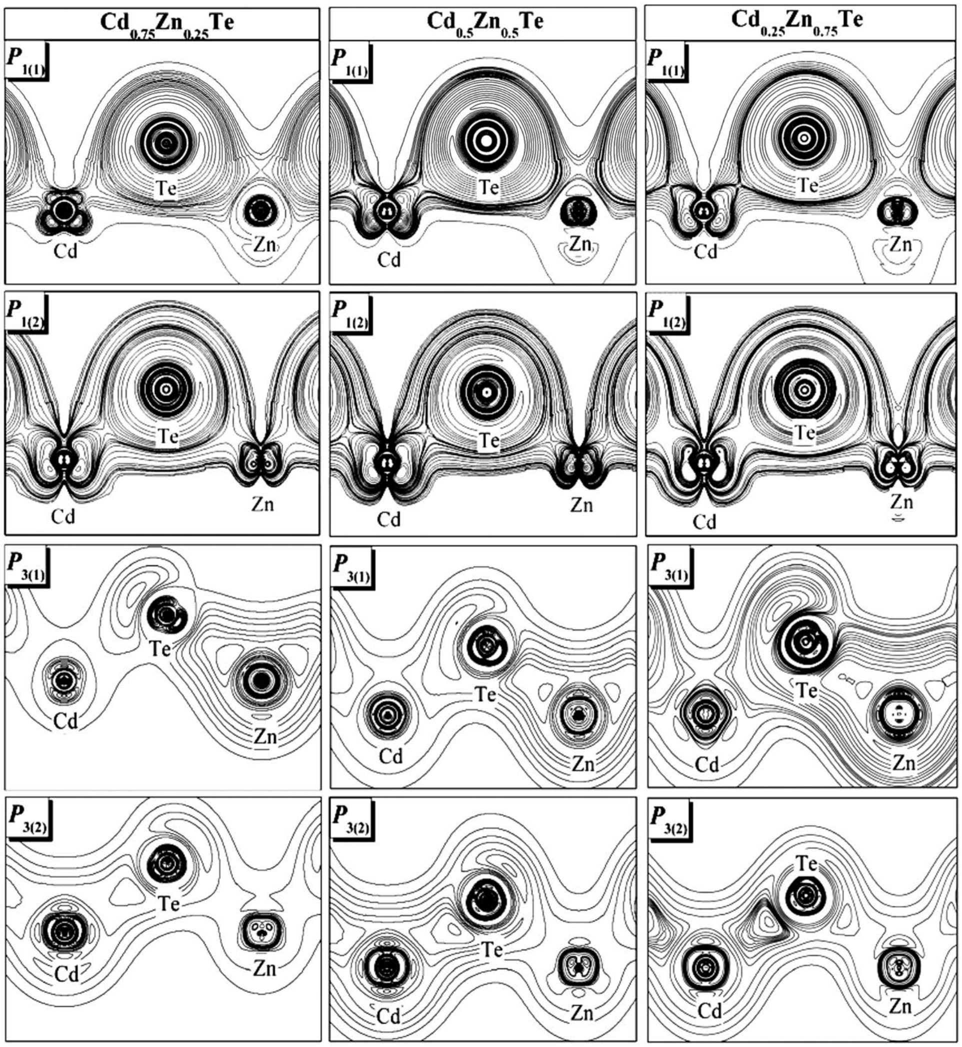

FIG. 3. Electronic charge densities associated with featured peaks in total DOS for relaxed $Cd_{1-x}Zn_xTe$ alloys. In the $P_{1(1)}$ peak, charges are localized on the $Te_{(2)}$ site in $x=0.25$ case and on the $Te_{(2)}$ site in $x=0.75$ case, whereas in $P_{1(2)}$ region, charges have amplitudes on the $Te_{(1)}$ site in the $x=0.25$ case and on the $Te_{(2)}$ site in the $x=0.75$ case. For $Cd_{0.5}Zn_{0.5}Te$ alloy, charges are localized both on the $Te_{(1)}$ site and on the $Te_{(2)}$ site in the $P_{1(1)}$ and $P_{1(2)}$ peaks. Distinguishing bonding is related to Zn-Te bond within the $P_{3(1)}$ peak and Cd-Te bond within the $P_{3(1)}$ and $P_{3(2)}$ peaks, respectively. The charge density is given in units of $10^{-4}\ e/\text{a.u.}^3$ in the $P_{1(1)}$ and $P_{1(2)}$ regions and $5\times10^{-3}\ e/\text{a.u.}^3$ in the $P_{3(1)}$ and $P_{3(2)}$ regions; the step size is 2.

ing the outmost *d* electrons on the same footing as other valence electrons. On the contrary, the calculations[57,58] without explicitly including *d* orbitals as valence states (the cation *d* orbitals are frozen) presented an unphysical trend in *d*-orbital energies and cohesive energies of ZnTe and CdTe. Our results hence support the arguments well established by Wei and Zunger[55] that the cation *d* orbital has direct effects on the atomic valence *s* and *p* electrons for ZnTe and CdTe and thus the valence *d* levels cannot be neglected in Zn and Cd, otherwise substantial discrepancies will occur.

For the reason above, the orbital energy of the Zn 3*d* states is expected to be higher than that of the Cd 4*d* states. Thus, with the decrease of symmetry from $T_d$ in zinc-blende binaries to $C_{3v}$ or $D_{2d}$ in quasi-zinc-blende alloys, the difference of the metal *d* orbital in energy leads to the splitting of the $P_2$ peak. This splitting is unchanged in going from the prerelaxed to the relaxed structures owing to undistorted metal sublattices.

From the overall total atomic DOS in Fig. 2, one can see the energy coincidence of the cation valence *s* and *p* states and the anion valence *p* states in the $P_3$ and $P_5$ regions. The calculated atomic-orbital energies of Zn and Cd show that the energy difference of the *s* orbitals is larger than that of the *p* orbitals (we find −1.36 and −1.43 eV for Zn 4*p* and Cd 5*p*, whereas −5.98 and −5.66 eV for Zn 4*s* and Cd 5*s*, respectively). Hence, for a fixed (unrelaxed) cation-anion bond length, the energy levels of the $P_3$ and $P_5$ states are dominated by the order of the cation *s*-orbital energies, e.g., the two splitting components associated with deeper $ZnTe_{(2)}$-like $P_{3(1)}$ and $P_{5(1)}$ peaks and shallower $CdTe_{(1)}$-like $P_{3(2)}$ and $P_{5(2)}$ peaks. However, we notice that the $P_3$ splitting becomes more distinct, while the $P_5$ splitting is elimi-

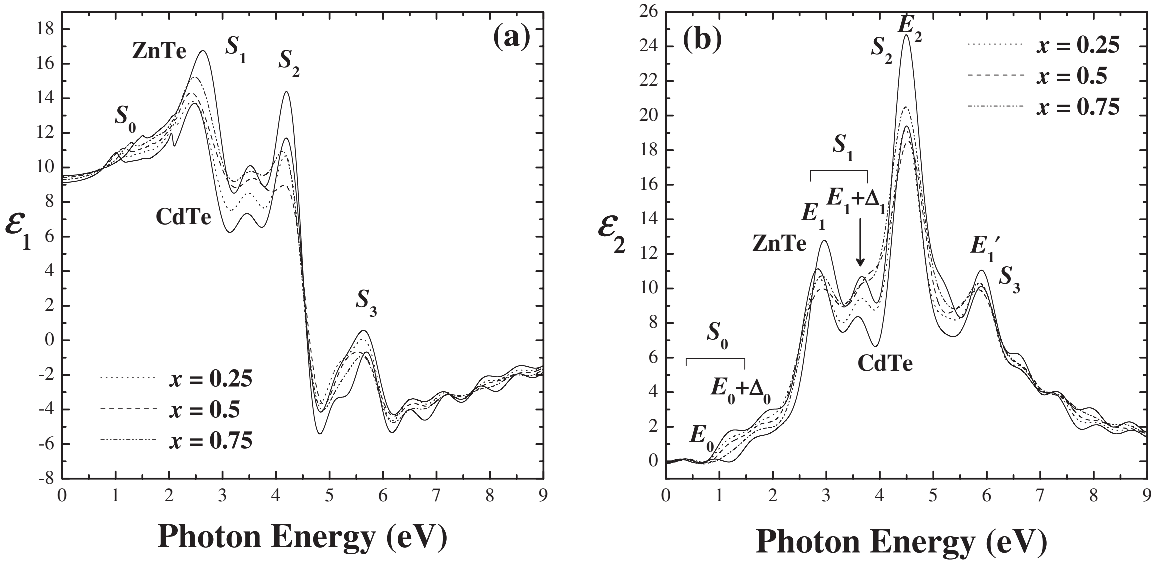

FIG. 4. Calculated real ($\varepsilon_1$) and imaginary ($\varepsilon_2$) spectra parts of the frequency dependent dielectric functions for relaxed $Cd_{1-x}Zn_xTe$ alloys as well as binary constituents. All peak positions shift toward the lower energies by around 1 eV with respect to other theoretical results owing to the underestimation of band gaps in this work. Four features labeled $S_0$, $S_1$, $S_2$, and $S_3$ exhibited in both $\varepsilon_1$ and $\varepsilon_2$ spectra are discussed in the text. The values of the fine structures in each of these regions are tabulated in Table III with a comparison with experimental and theoretical data.

nated in going from the prerelaxed structures to the postrelaxed structures for $Cd_{1-x}Zn_xTe$ alloys. This is a clear manifestation of structural relaxation effect significant in these two regions.

Since $P_3$ and $P_5$ are $sp^3$ bond centered and antibond centered states, respectively, they respond primarily to changes in bond lengths through their deformation potentials: when bonds are shortened, bonding (antibonding) states move to deeper (shallower) binding energies; inversely, when bonds are elongated, bonding (antibonding) states move to shallower (deeper) binding energies.[25] Upon relaxation, the Zn-Te bond is compressed whereas the Cd-Te bond is stretched; thereby, the $P_{3(1)}$ $[P_{5(1)}]$ peak is displaced to a lower (higher) energy level, whereas the $P_{3(2)}$ $[P_{5(2)}]$ peak is displaced to a higher (lower) energy level. This opposite level shift acts to increase the energy separation between bonding CdTe-like $[P_{3(2)}]$ and ZnTe-like $[P_{3(1)}]$ states, but reduces the separation between antibonding CdTe-like $[P_{5(2)}]$ and ZnTe-like $[P_{5(1)}]$ states. Similar results have been obtained for $Cd_{0.5}Zn_{0.5}Te$.[25] Moreover, note that the absolute magnitude of bond-length deformation is isotropic for $Cd_{0.5}Zn_{0.5}Te$ while anisotropic for Cd-rich and Zn-rich cases, which leads to a more effective relaxation-induced shift [i.e., a more remarkable increase (reduction) in the level separation for the $P_3$ ($P_5$) states, and consequently, a more notable broadening (narrowing) $P_3$ ($P_5$) shoulder with respect to the situation in the prerelaxed structures] for $Cd_{0.5}Zn_{0.5}Te$ relative to $Cd_{0.75}Zn_{0.25}Te$ and $Cd_{0.25}Zn_{0.75}Te$ (see Fig. 2). The energy splitting of $P_3$ in $Cd_{0.5}Zn_{0.5}Te$ is 0.41 eV, in agreement with the predictions of the SQS model[25,55,59] for explaining the increased linewidth of the valence-band photoemission spectrum near the $X_6$ point.[26]

Figure 3 depicts the electronic charge densities in the $P_3$ region, clear exhibiting distinct Zn-Te bonding in the $P_{3(1)}$ states and Cd-Te bonding in the $P_{3(2)}$ states, respectively. The changes in the bonding character in terms of alloy composition correspond to the trends in the relaxation-induced shifts as discussed above.

The $P_4$ and $P_6$ regions have $p$-like character as seen from the overall total atomic DOS in Fig. 2. The maximum in the $P_4$ region ($\Gamma_{7v}$ state) has over ~70% anion $p$ states. The delocalization of $p$ electrons corresponds to atomic independent extended states in these regions. It therefore seems that the ionic relaxations play less important role within these two regions.

### C. Optical properties of $Cd_{1-x}Zn_xTe$ alloys

We present in this section our results of the interband optical properties in the $Cd_{1-x}Zn_xTe$ system and explain features related to the band structures. Here, direct rather than indirect interband transitions are considered, and only the first diagonal element of $\varepsilon(\omega)$ is presented owing to negligible anisotropic off-diagonal elements in the cubic $Cd_{1-x}Zn_xTe$ system.

In Fig. 4, we show the calculated real and imaginary parts of the frequency dependent dielectric functions for the relaxed $Cd_{1-x}Zn_xTe$ ternaries as well as binary constituents up to photon energy of 9 eV. The general patterns of the $\varepsilon(\omega)$ curves of $Cd_{1-x}Zn_xTe$ systems are seen to be rather similar, indicating the underlying generic character in their band structures. Four features labeled $S_0$, $S_1$, $S_2$, and $S_3$ are exhibited in both $\varepsilon_1$ and $\varepsilon_2$ spectra. For the $S_0$ region in the $\varepsilon_2$ spectrum, the $E_0$ threshold and its adjacent $E_0+\Delta_0$ shoulder coincide with the interband transitions at $\Gamma$. With the band gap opening up away from $\Gamma$, three experimentally observed Van Hove singularity structures occur, namely, double peaks $E_1$ below 3.0 eV, $E_1+\Delta_1$ around 3.65 eV in the $S_1$ region, and the main peak $E_2$ in the $S_2$ region. The double peaks

TABLE III. Comparison of the transition energies at the critical structures discussed in the imaginary part of the dielectric function of the $Cd_{1-x}Zn_xTe$ system with data from spectroscopic ellipsometry measurements and empirical pseudopotential calculations for binary constituents. The additional part of this table illustrates the calculated static dielectric $\varepsilon_1(0)$, compared with available experimental and theoretical data.

| | Transition energies $\varepsilon_2$ (eV) | | | | | | | | | | | | | |
|---|---|---|---|---|---|---|---|---|---|---|---|---|---|---|
| | Spectroscopic ellipsometry measurements[a] | | | | | Numerical model analysis based on experiments | | | | This work and empirical pseudopotential method | | | | |
| Region | $x=0$ | $x=0.25$ | $x=0.5$ | $x=0.75$ | $x=1.0$ | $x=0$ | $x=0.25$ | $x=0.5$ | $x=1.0$ | $x=0$ | $x=0.25$ | $x=0.5$ | $x=0.75$ | $x=1.0$ |
| $E_0$ | 1.6 | 1.8 | 1.9 | 2.1 | 2.3 | $1.58^{b}$<br>$1.52^{f}$ | $1.66^{f}$ | $1.85^{f}$ | $2.28^{c}$<br>$2.27^{f}$ | $1.51^{d}$<br>0.74 | 0.83 | 0.9 | 1.05 | $2.21^{e}$<br>1.23 |
| $E_0+\Delta_0$ | 2.6 | 2.7 | 2.9 | 3.0 | 3.2 | $2.55^{b}$<br>2.45 | $2.58^{f}$ | $2.78^{f}$ | $3.19^{f}$ | 1.84 | 2.06 | 2.26 | 2.37 | $3.14^{e}$<br>2.51 |
| $E_1$ | 3.6 | 3.6 | 3.7 | 3.7 | 3.8 | $3.55^{b}$<br>$3.62^{f}$ | $3.38^{f}$ | $3.43^{f}$ | $3.58^{c}$<br>$3.63^{f}$ | $3.16^{d}$<br>2.84 | 2.86 | 2.91 | 2.92 | $3.64^{e}$<br>2.95 |
| $E_1+\Delta_1$ | 4.1 | 4.2 | 4.2 | 4.3 | 4.3 | $4.13^{b}$<br>$3.96^{f}$ | $3.98^{f}$ | $4.05^{f}$ | $4.14^{c}$<br>$4.23^{f}$ | $3.64^{d}$<br>3.58 | 3.65 | 3.65 | 3.65 | $4.21^{e}$<br>3.66 |
| $E_2$ | 5.1 | 5.2 | 5.2 | 5.2 | 5.2 | $5.13^{b}$<br>$5.04^{f}$ | $4.98^{f}$ | $5.15^{f}$ | $5.23^{c}$<br>$5.28^{f}$ | $4.83^{d}$<br>4.50 | 4.48 | 4.51 | 4.48 | $5.26^{e}$<br>4.49 |
| $E_1'$ | | | | | | | | | | $5.76^{d}$<br>5.90 | 5.85 | 5.86 | 5.86 | $6.72^{e}$<br>5.89 |

| | Static dielectric $\varepsilon_1(0)$ | | | | |
|---|---|---|---|---|---|
| | $x=0$ | $x=0.25$ | $x=0.5$ | $x=0.75$ | $x=1.0$ |
| Experiment | 7.4<br>7.2 | | | | 7.28 |
| Theory | 9.11<br>$9.02^{d}$ | | | | 5.24 |
| This work | $9.52^{g}$ | 9.48 | 9.42 | 9.31 | $9.13^{g}$ |

[a] Reference 44.
[b] Reference 35.
[c] Reference 36.
[d] Reference 42.
[e] Reference 40.
[f] Reference 45.
[g] Reference 43.

arise from the transitions extending $\Lambda_{3v}$-$\Lambda_{1c}$ toward $L$ with spin-orbital coupling, while the $E_2$ peak at 4.5 eV is attributed to the transitions along the $\Delta$ direction (the $\Delta_{5v}$-$\Delta_{1c}$ near $X$, $X_{5v}$-$X_{1c}$, and $K_{2v}$-$K_{1c}$ transitions) which also extend near the outer portions toward $\Lambda$ and $\Sigma$ directions. Finally, some descending setback-type structures in the $S_3$ region indicate a decrease in the oscillator strength away from the $\Lambda$ direction where the valence and conduction bands are less parallel to each other. Compared with the available results for binaries,[60] an overall topological resemblance is found in the present $\varepsilon(\omega)$ curves. However, the band gaps in the framework of density functional theory are underestimated so that all peak positions are shifted toward the lower energies by around 1 eV (see Table III) in our results with respect to the other theoretical results which involved the extra potentials to compensate the too low gap values[42] or adjusted pseudopotential form factor to reproduce experiments.[40]

For ternaries, the calculated $\varepsilon(\omega)$ curves are bounded by the curves of the two limiting binaries and have three interesting features: (1) The transition energy increases linearly with the alloy composition. (2) The magnitude of $\varepsilon_2$ exhibits a nonlinear dependence on the alloy composition. The $S_0$ structure is observed to be more pronounced at the lower composition. This trend can be understood from the alloying effect on the evolution of band structures: as the composition increases, the $P_{S(1)}$ band levels steadily move away from the top of the valence band (as discussed in Sec. III B), causing a reduction in the parallel property of the bands near the critical point $\Gamma$, which thereby reduces the direct contribution from the joint density of states to the magnitude of the $\varepsilon_2$. A similar trend is found in the $E_1$ peak until the composition exceeds 0.5, and then the magnitude of $\varepsilon_2$ jumps sharply and increases with the increased composition. The trend in the $E_1$ peak continues across the remaining regions except for the

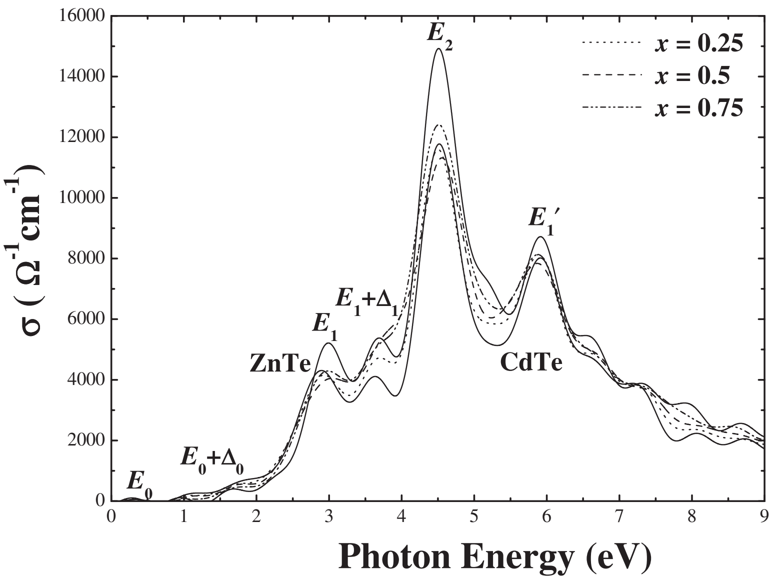

FIG. 5. Calculated optical conductivity spectra for the $Cd_{1-x}Zn_xTe$ system. Six absorption structures labeled $E_0$, $E_0+\Delta_0$, $E_1$, $E_1+\Delta_1$, $E_2$, and $E_l'$ are identical with the structures given in $\varepsilon(\omega)$ curves.

$E_1+\Delta_1$ peak, where the magnitude of $\varepsilon_2$ increases through the compositions. Note that the magnitude for the $E_1$ and $E_1+\Delta_1$ transitions is underestimated relative to the experiment[44] probably due to the absence of the excitonic effect[61] in the present calculations, but their transition energies agree with the experimental data when the band-gap correction is included (see Table III). In the $S_2$ structure, the magnitude for the $E_2$ transition is significantly overestimated compared with the measurements[35,36,44] (taken without corrections for the surface roughness), which is consistent with the previous theoretical results. (3) The values of static dielectric $\varepsilon_1(0)$ at the zero frequency limit are listed in Table III. They are much greater than those found in the other first-principles calculations,[43,44] especially for ZnTe, as a result of the increased gap underestimation in the present work as mentioned before. We can see that the values of $\varepsilon_1(0)$ decrease slowly when $x$ increases to 0.5 but then decrease sharply. This is understandable from the previous findings[57,62,63] that the precise $\varepsilon_1(0)$ values depend not only on band gaps but also on the local-field effect, and the latter is usually neglected in first-principles calculations. In this case, the neglect of this effect seems more significant at low composition, greatly compensating for the reduction of the $\varepsilon_1(0)$. However, at high composition, the predominant widened band gap results in a sharp decrease in $\varepsilon_1(0)$. The above information on the transition on the critical points is also illustrated by the calculated optical conductivity spectra in Fig. 5. Six absorption structures labeled $E_0$, $E_0+\Delta_0$, $E_1$, $E_1+\Delta_1$, $E_2$, and $E_1'$ are identical with the structures given in the $\varepsilon(\omega)$ curves. They cover a wide range from visible bands ($E_0$ and $E_0+\Delta_0$) to ultraviolet bands ($E_1$, $E_1+\Delta_1$, and $E_2$), and to a high-energy radiation band ($E_1'$) by considering a compensation of band gap of 1 eV. Generally, $Cd_{1-x}Zn_xTe$ alloys have high absorption in the near ultraviolet and high-energy radiation regions.

It is interesting to extend our investigations of the optical transitions to higher photon energies in order to analyze the reflectivity and the energy-loss functions[64] (Fig. 6). The calculated reflectivity reaches a maximum value of around 55% at the $E_2$ peak, whereas the experimental value[35,36,44] does not exceed 50% at this energy. A similar trend is apparent by a comparison of calculations with experiments for many other semiconductors.[65] Such overestimation is probably due to the extrapolation in calculating $\varepsilon_1$ through the Kramer-Kronig relations at high frequencies, and on the other side, the surface roughness is expected to weaken the reflectivity more or less in experiment measurements, which further deteriorates the discrepancy in the experiments and calculations of the reflectivity at $E_2$.

## IV. CONCLUSIONS

In this work, we have investigated the ionic relaxations of $Cd_{1-x}Zn_xTe$ alloys in detail. Besides some conclusions drawn

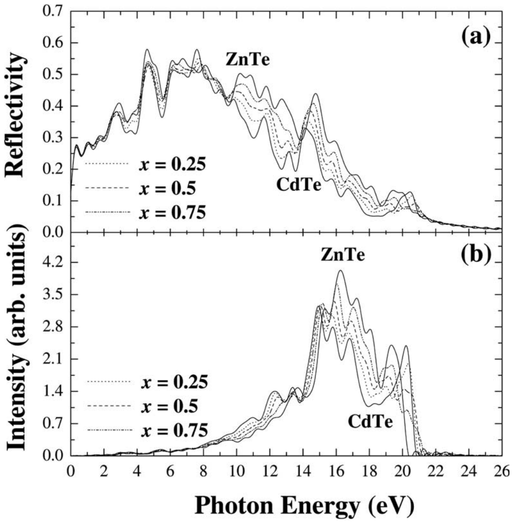

FIG. 6. Calculated (a) reflectivity and (b) energy-loss spectra for the $Cd_{1-x}Zn_xTe$ system. The most remarkable descending branch between 14 and 20 eV in the reflectivity spectra coincides with a strong peak group in the energy-loss spectra as a result of the collective plasma resonance. The plasma minimum shifts toward higher energies with the increase of alloy composition.

by previous experiments and theories, such as the conserved bond lengths and the outward expansion of the anion sublattice, other results are also obtained. The relaxations of $Te^{2-}$ rather than those of $Cd^{2+}$ and $Zn^{2+}$ are the primary contributors to the alloying process. The differences in the ionicity of $Cd^{2+}$ and $Zn^{2+}$ and their configurations around $Te^{2-}$ are responsible for the different relaxation behaviors for ternary compounds. We have also investigated the alloying effect on the electronic states based on the relaxation behaviors of $Te^{2-}$. Our results support the previous systematic analyses by taking the quasirandom structure. The splitting of the Te-localized $P_1$ region results from the deformation of $Te_{(1)}$- and $Te_{(2)}$-based tetrahedrons, while in the $P_3$ and $P_5$ regions the bond-length relaxation operates. Finally, the band structures obtained here were used to determine the optical functions. We find that the transition energy in the $\varepsilon_2(\omega)$ spectra increases linearly with the composition, whereas the magnitude of $\varepsilon_2$ exhibits a nonlinear dependence on the alloy composition. In addition, the values of $\varepsilon_1(0)$ decrease slowly when $x$ increases to 0.5 but then decrease sharply, and the plasma minimum shifts toward higher energies with the increase of the alloy composition. As compared with the available experimental and theoretical results, there is an overall topological resemblance in the present $\varepsilon(\omega)$ spectra when the band-gap correction is included.

## ACKNOWLEDGMENTS

The authors would like to thank R. Bruce King and Jijun Zhao for useful discussions and comments on this paper. This work was financially supported by the Chinese National Key Basic Research Special Fund, the Key Fund of the Chinese National Science Foundation (No. 10234040), the Chinese National Science Foundation (No. 60221502 and No. 60476040), the Key Foundation of Shanghai Commission of Science and Technology (No. 02DJ14006), and the Creative Foundation of Shanghai Institute of Technical Physics (No. C2-5). The authors are also grateful to the Shanghai Supercomputer Center.

---

[*] Corresponding authors.

[†] xschen@mail.sitp.ac.cn

[‡] luwei@mail.sitp.ac.cn

[1] B. Samanta, A. K. Chaudhuri, S. L. Sharma, and U. Pal, J. Appl. Phys. **75**, 2733 (1994).

[2] A. Parsons, S. Barthelemy, F. B. Birsa, N. Gehrels, J. Naya, J. Odom, S. Singh, C. Stahl, J. Tueller, and B. Teagarden, Proc. SPIE **2806**, 432 (1996).

[3] T. Watanabe, H. Sekiya, K. Takahisa, M. Tanikawa, and Y. Ito, Nucl. Instrum. Methods Phys. Res. A **436**, 155 (1999).

[4] S. Miyajima, K. Imagawa, and M. Matsumoto, Med. Phys. **29**, 1421 (2002).

[5] T. E. Schlesinger, J. E. Toney, R. B. Ames, L. Franks, and H. Yoon, Mater. Sci. Eng., R. **32**, 103 (2001).

[6] Muren Chu, Sevag Terterian, David Ting, C. C. Wang, H. K. Gurgenian, and Shoghig Mesropian, Appl. Phys. Lett. **79**, 2728 (2001).

[7] G. Q. Li, W. Q. Jie, Z. Gu, and H. Hua, J. Cryst. Growth **263**, 332 (2004).

[8] C. C. Wang, J. Vac. Sci. Technol. B **9**, 1740 (1991).

[9] T. S. Lee, K. K. Choi, Y. T. Jeong, and K. K. Kim, J. Electron. Mater. **26**, 552 (1997).

[10] W. E. Spicer, J. A. Silberman, J. Morgen, I. Lindau, J. A. Wilson, A.-B. Chen, and A. Sher, Phys. Rev. Lett. **49**, 948 (1982).

[11] S. L. Bell and S. Sen, J. Vac. Sci. Technol. A **3**, 112 (1985).

[12] T. M. Duc, C. Hsu, and J. P. Faurie, Phys. Rev. Lett. **58**, 1127 (1987).

[13] A. Sher, M. A. Berding, and M. van Schilfgaarde, J. Cryst. Growth **86**, 15 (1988).

[14] C. K. Shih, A. K. Wahi, I. Lidau, and W. E. Spicer, J. Vac. Sci. Technol. A **6**, 2640 (1988).

[15] D. Comedi and R. Kalish, Phys. Rev. B **46**, 15844 (1992).

[16] N. T. Pelekanos, P. Peyla, Le Si Dang, H. Mariette, P. H. Jouneau, A. Tardot, and N. Magnea, Phys. Rev. B **48**, 1517 (1993).

[17] N. Motta *et al.*, Solid State Commun. **53**, 509 (1985).

[18] K. Beshah, D. Zamir, P. Becla, P. A. Wolff, and R. G. Griffin, Phys. Rev. B **36**, 6420 (1987).

[19] D. W. Niles and H. Höchst, Phys. Rev. B **46**, 1498 (1992).

[20] D. W. Niles and H. Höchst, J. Vac. Sci. Technol. A **10**, 1526 (1992).

[21] A. Zin and E. A. Stern, Phys. Rev. B **31**, 4954 (1985).

[22] D. W. Niles, D. Rioux, and H. Höchst, Phys. Rev. B **46**, 12547 (1992).

[23] A. Balzarotti, N. Motta, A. Kisiel, M. Zimnal-Starnawska, M. T. Czyznyk, and M. Podgórny, Phys. Rev. B **31**, 7526 (1985).

[24] S.-H. Wei, L. G. Ferreira, James E. Bernard, and Alex Zunger, Phys. Rev. B **42**, 9622 (1990).

[25] S.-H. Wei and A. Zunger, Phys. Rev. B **43**, 1662 (1991).

[26] D. W. Niles and H. Höchst, Appl. Phys. Lett. **64**, 1147 (1994).

[27] J. C. Mikkelsen and J. B. Boyce, Phys. Rev. Lett. **49**, 1412 (1982); Phys. Rev. B **28**, 7130 (1983); N. Motta, A. Balzarotti, P. Letardi, A. Kisiel, M. T. Czyzyk, M. Zimnal-Starnawska, and M. Podgorny, J. Cryst. Growth **72**, 205 (1985).

[28] O. Castaing, J. T. Benhlal, R. Granger, and R. Triboulet, J. Cryst. Growth **159**, 1112 (1996).

[29] K. Prabakar, Sa. K. Narayandass, and D. Mangalaraj, J. Alloys Compd. **364**, 23 (2004).

[30] S. M. Johnson, S. Sen, W. H. Konkel, and M. H. Kalisher, J. Vac. Sci. Technol. B **9**, 1897 (1991).

[31] M. Sridharan, Sa. K. Narayandass, D. Mangalaraj, and Hee Chul Lee, J. Alloys Compd. **346**, 100 (2002).

[32] K. Prabakar, M. Sridheran, Sa. K. Narayandass, D. Mangalaraj, and Vishnu Gopal, Thin Solid Films **424**, 66 (2003).

[33] K. Prabakar, S. Venkatachalam, Y. L. Jeyachandran, Sa. K. Narayandass, and D. Mangalaraj, Sol. Energy Mater. Sol. Cells **81**, 1 (2004).

[34] S. Adachi and K. Sato, Jpn. J. Appl. Phys., Part 1 **31**, 3907 (1992).

[35] T. Kimura and S. Adachi, Jpn. J. Appl. Phys., Part 1 **32**, 2740 (1993).

[36] K. Sato and S. Adachi, Jpn. J. Appl. Phys., Part 1 **73**, 926 (1993).

[37] S. Adachi, T. Kimura, and N. Suzuki, J. Appl. Phys. **74**, 3435 (1993).

[38] K. Saito, A. Ebina, and T. Takahashi, Solid State Commun. **11**, 841 (1972).

[39] V. V. Sobolev, O. G. Maksimova, and S. G. Kroitoru, Phys. Status Solidi B **103**, 499 (1981).

[40] John P. Walter and Marvin L. Cohen, Phys. Rev. B **1**, 2661 (1970).

[41] D. J. Chadi, John P. Walter, and Marvin L. Cohen, Phys. Rev. B **5**, 3058 (1972).

[42] M. Alouani, L. Brey, and N. E. Christensen, Phys. Rev. B **37**, 1167 (1988).

[43] Ming-Zhu Huang and W. Y. Ching, Phys. Rev. B **47**, 9449 (1993).

[44] S. Adachi and T. Kimura, Jpn. J. Appl. Phys., Part 1 **32**, 3496 (1993).

[45] O. Casting, J. T. Benhlal, and R. Granger, Eur. Phys. J. B **7**, 563 (1999).

[46] A. H. MacDonald, W. E. Pickett, and D. D. Koelling, J. Phys. C **13**, 2675 (1980); W. E. Pickett, A. J. Freeman, and D. D. Koelling, Phys. Rev. B **23**, 1266 (1981).

[47] P. Blaha, K. Schwarz, G. K. H. Madsen, D. Kvasnicka, and J. Luitz, WIEN2K, an augmented plane wave+local orbital program for calculating crystal properties, Karlheinz Schwarz, Technische Universität Wien, Austria, 2001.

[48] John P. Perdew, Kieron Burke, and Matthias Ernzerhof, Phys. Rev. Lett. **77**, 3865 (1996).

[49] *Numerical Data and Functional Relationships in Science and Technology*, edited by K.-H. Hellwege and O. Madelung, Landolt-Börnstein, New Series, Group III, Vol. 17, Pt. A (Springer, New York, 1982); *Numerical Data and Functional Relationships in Science and Technology*, edited by K.-H. Hellwege and O. Madelung, Landolt-Börnstein, New Series, Group III, Vol. 22, Pt. A (Springer, New York, 1982).

[50] F. D. Murnaghan, Proc. Nat. Acad. Sci. U.S.A. **30**, 244 (1944). The derivation of the Murnaghan's EOS is cited as follows: To begin with, we consider the pressure

$$P = -\left(\frac{\partial E}{\partial V}\right)_S \tag{1}$$

and the bulk modulus

$$B = -V\left(\frac{\partial P}{\partial V}\right)_T. \tag{2}$$

Experimentally, the bulk modulus pressure derivative

$$B' = \left(\frac{\partial B}{\partial P}\right)_T \tag{3}$$

is found to change little with pressure. If we take $B' = B_0'$ to be a constant, then

$$B = B_0 + B_0' P, \tag{4}$$

where $B_0$ is the value of $B$ when $P=0$. We may equate this with Eq. (2) and rearrange as

$$\frac{dV}{V} = -\frac{dP}{B_0 + B_0' P}. \tag{5}$$

Integrating this results in

$$P(V) = \frac{B_0}{B_0'}\left[\left(\frac{V_0}{V}\right)^{B_0'} - 1\right] \tag{6}$$

or equivalently

$$V(P) = V_0\left(1 + B_0'\frac{P}{B_0}\right)^{-1/B_0'}. \tag{7}$$

Substituting Eq. (6) into $E = E_0 - \int P dV$ then results in the equation of state for energy,

$$E(V) = E_0 + \frac{B_0 V}{B_0'}\left[\frac{\left(\frac{V_0}{V}\right)^{B_0'}}{B_0' - 1} + 1\right] - \frac{B_0 V_0}{B_0' - 1}. \tag{8}$$

[51] Rici Yu, D. Singh, and H. Krakauer, Phys. Rev. B **43**, 6411 (1991).

[52] B. Kohler, S. Wilke, M. Scheffler, R. Kouba, and C. Ambrosch-Draxl, Comput. Phys. Commun. **94**, 31 (1996).

[53] A. Continenza and S. Massidda, Phys. Rev. B **50**, 11949 (1994).

[54] J. L. Martins and A. Zunger, Phys. Rev. B **30**, 6217 (1984).

[55] S.-H. Wei and A. Zunger, Phys. Rev. B **37**, 8958 (1988).

[56] S.-H. Wei, S. B. Zhang, and A. Zunger, J. Appl. Phys. **87**, 1304 (2000).

[57] C. F. Fischer, At. Data **4**, 301 (1972); W. A. Harrison, Phys. Rev. B **24**, 5835 (1981); W. A. Harrison, Phys. Rev. B **31**, 2121 (1985).

[58] K. C. Hass and D. Vanderbilt, J. Vac. Sci. Technol. A **5**, 3019 (1987).

[59] A. Zunger, S.-H. Wei, L. G. Ferreira, and J. E. Bernard, Phys. Rev. Lett. **65**, 353 (1990).

[60] W. A. Harrison, *Electronic Structure and the Properties of Solids* (Freeman, San Francisco, 1980).

[61] W. Hanke and L. J. Sham, Phys. Rev. B **21**, 4656 (1980).

[62] C. S. Wang and B. M. Klein, Phys. Rev. B **24**, 3393 (1981).

[63] Z. H. Levine and D. C. Allan, Phys. Rev. Lett. **63**, 1719 (1989).

[64] G. Cappellini, S. Bouette-Russo, B. Amadon, C. Noguera, and F. Finocchi, J. Phys.: Condens. Matter **12**, 3671 (2000).

[65] C. S. Wang and B. M. Klein, Phys. Rev. B **24**, 3417 (1981).